Engineering 22 (2023) 171–184

Contents lists available at ScienceDirect

Engineering

journal homepage: www.elsevier.com/locate/eng

Research
Green Plant Protection Innovation—Article

Fingerprint Spectral Signatures Revealing the Spatiotemporal Dynamics of Bipolaris Spot Blotch Progression for Presymptomatic Diagnosis

Fengle Zhu [a,#], Zhenzhu Su [b,#], Alireza Sanaeifar [c], Anand Babu Perumal [c], Mostafa Gouda [c,d], Ruiqing Zhou [c], Xiaoli Li [c,*], Yong He [c]

[a] College of Mechanical Engineering, Zhejiang University of Technology, Hangzhou 310023, China
[b] State Key Laboratory for Rice Biology, Institute of Biotechnology, Zhejiang University, Hangzhou 310058, China
[c] College of Biosystems Engineering and Food Science, Zhejiang University, Hangzhou 310058, China
[d] Department of Nutrition and Food Science, National Research Centre, Cairo 12311, Egypt

ARTICLE INFO

Article history:
Received 3 December 2021
Revised 19 September 2022
Accepted 13 October 2022
Available online 28 November 2022

Keywords:
Hyperspectral imaging
Fingerprint spectral signatures
Spot blotch
Leaf lesion progression
Presymptomatic diagnosis
Biochemical indicators

ABSTRACT

Plant pathogens continuously impair agricultural yields and food security. Therefore, the dynamic characterization of early pathogen progression is crucial for disease monitoring and presymptomatic diagnosis. Hyperspectral imaging (HSI) has great potential for tracking the dynamics of initial infected sites for presymptomatic diagnosis; however, no related studies have extracted fingerprint spectral signatures (FSSs) that can capture diseased lesions on leaves during the early infection stage *in vivo* or investigated the detection mechanism of HSI relating to the host biochemical responses. The FSSs denote unique and representative spectral signatures that characterize a specific plant disease. In this study, the FSSs of spot blotch on barley leaves inoculated with *Bipolaris sorokiniana* were discovered to characterize symptom development for presymptomatic diagnosis based on time-series HSI data analysis. The early spectral and biochemical responses of barley leaves to spot blotch progression were also investigated. The full-spectrum FSSs were physically interpretable and could capture the unique characteristics of chlorotic and necrotic tissues along with lesion progression, enabling the *in situ* visualization of the spatiotemporal dynamics of early plant–pathogen interactions at the pixel level. Presymptomatic diagnosis of spot blotch was achieved 24 h after inoculation—12 h earlier than the traditional polymerase chain reaction (PCR) assay or biochemical measurements. To uncover the mechanism of HSI presymptomatic diagnosis, quantitative relationships between the mean spectral responses of leaves and their biochemical indicators (chlorophylls, carotenoids, malondialdehyde (MDA), ascorbic acid (AsA), and reduced glutathione (GSH)) were developed, achieving determination coefficient of prediction set (R_p^2) > 0.84 for regression models. The overall results demonstrated that, based on the association between HSI and *in vivo* plant-trait alterations, the extracted FSSs successfully tracked the spatiotemporal dynamics of bipolaris spot blotch progression for presymptomatic diagnosis. Tests of this methodology on other plant diseases demonstrated its remarkable generalization potential for the early control of plant diseases.

1. Introduction

Plant pathogens impair the yield and quality of agricultural production. The fungal pathogen *Bipolaris sorokiniana* (*B. sorokiniana*; teleomorph: *Cochliobolus sativus*) invades a number of host plants, including wheat (*Triticum aestivum*), barley (*Hordeum vulgare*), rice (*Oryza sativa*), and maize (*Zea mays*) [1,2]. *B. sorokiniana* is prevalent in the warm, humid regions of Asia, Africa, America, and Europe [3,4]. The diseases caused by this fungus include foliar spot blotch, root rot, and black point on grains [1], leading to yield losses of 2%–30% and up to 100% in South Asia and to losses of 10%–20% in Scotland, Canada, and Brazil [5–7]. Among these diseases, leaf spot blotch is considered to be highly important in cereal crops such as wheat and barley [2,3,8,9], affecting nearly

* Corresponding author.
E-mail address: xiaolili@zju.edu.cn (X. Li).
# These authors contributed equally to this work.

https://doi.org/10.1016/j.eng.2022.10.006

1.2×10^7 hm^2 in South Asia's intensive cropping systems [1]. Leaf spot blotch is characterized by dark brown necrotic lesions surrounded by chlorotic halos, leading to photosynthesis reduction, cell death, and accelerated leaf senescence [1,2]. Because of its high contagiosity, which is facilitated by wind and rain transmission [3], and the potential progression into spikes resulting in grain shriveling and embryo discoloration [3,4], early diagnosis of spot blotch—even at the presymptomatic (i.e., without visible symptoms) stage—plays a vital role in preventing large-scale disease outbreaks and ensuring global food security.

For the early diagnosis of foliar disease, visual monitoring by experts remains the most common method in field crops and horticulture [10]. However, visual monitoring is labor-intensive, time-consuming, subjective, and prone to errors, as early plant–pathogen interaction sites are sometimes invisible [10], especially when fungi colonize host tissue intercellularly under low light intensity [1]. The conventional polymerase chain reaction (PCR) assay is considered to be the most sensitive diagnostic approach; however, this assay is tedious and destructive, and its detection accuracy is affected by sampling and uneven pathogen distribution inside leaves, particularly at presymptomatic stages [11]. Therefore, a rapid and *in situ* approach is essential for accurately detecting spot blotch during the early infection stage.

Innovative optical sensing, such as hyperspectral imaging (HSI) [12,13], chlorophyll fluorescence imaging [14], and red–green–blue (RGB) imaging [15], is promising for the fast and non-invasive detection of early foliar diseases. HSI, also known as imaging spectroscopy, simultaneously acquires spectral and spatial information over hundreds of contiguous narrow spectral wavelengths to return an information-rich hyperspectral image [12]. HSI has been proven to be efficient in characterizing the subtle changes induced by early plant–pathogen interactions [10,16]. During *B. sorokiniana* invasion and plant early resistance, multiple processes occur, including the succession of necrotic and chlorotic tissues, appearance of fungal hyphae and conidia, oxidative damage burst with increased production of reactive oxygen species (ROS), accumulation of malondialdehyde (MDA) due to lipid peroxidation induced by elevated ROS, and enhanced antioxidant defense involving antioxidants such as ascorbic acid (AsA) and reduced glutathione (GSH) [1,10,17,18]. These physiological and biochemical alterations in plants are bound to change the optical reflectance properties of the early-infected tissues during the presymptomatic stage [10,19,20]. However, such minor spectral alterations pose great challenges for the accurate identification of infected but asymptomatic leaf samples [21,22], and advanced analysis methods must be combined.

Recently, many studies have validated the feasibility of HSI for early disease diagnosis in plant leaves or canopies from presymptomatic to symptomatic stages. Shuaibu et al. [23] employed an unsupervised band selection method to process hyperspectral images in order to distinguish various degrees of Marssonina blotch infection on apple leaves from asymptomatic to severe infection stages in indoor and outdoor settings. Arens et al. [24] classified healthy and asymptomatic sugar beet leaves inoculated with *Cercospora beticola* 4 days after inoculation (dai) based on HSI and conducted early metabolic profile analysis during plant–pathogen interaction. Gao et al. [25] validated the potential of HSI coupled with salient wavelength selection methods for the early detection of grapevine leafroll disease during asymptomatic and symptomatic stages. Healthy and powdery mildew disease-infected squash leaves were discriminated successfully at different disease development stages (asymptomatic, early, medium, and late) based on HSI and artificial intelligence algorithms [26]. In a similar HSI study on target spots and bacterial spots in tomato leaves by Abdulridha et al. [27], several disease developmental stages were identified manually, with disease detection accomplished at different stages. Although early foliar disease diagnosis was achieved in the above HSI studies, the spatiotemporal dynamics of plant–pathogen interaction sites—which play a vital role in monitoring the pattern of disease onset and progression—and the precise location of the presymptomatic lesions were not characterized.

To track the spatiotemporal dynamics of infected regions during initial pathogen infestation, some researchers have employed the pixel-wise visualization analysis of hyperspectral images, taking full advantage of HSI by considering the spatial resolution, which is conducive for early and robust disease monitoring. Using HSI and support vector machine (SVM) classifiers, Thomas et al. [28] visualized the spatial distribution of powdery mildew development in different barley cultivars as soon as the first symptoms were visible to the human eye at 12 dai. However, due to the mandatory manual annotation of visible diseased training pixels for supervised SVM training, presymptomatic infections were not detected in that study. In contrast, unsupervised learning can discover invisible diseased pixels. Thomas et al. [13] reported the earlier visualization of powdery mildew on barley leaves at 4 dai—2 days before symptoms became visible on RGB images—through principal component analysis (PCA) of measured reflection and transmission hyperspectral images. However, PCA is a linear combination of the original spectral bands, and cannot be used to solve the mixed problem of the pixel spectrum. Kuska et al. [29] adopted microscopic HSI combined with the simplex volume maximization (SiVM) method and likelihood ratio (LLRs) calculation to interpret and visualize the stages of pathogenesis from 3 to 14 dai with *Blumeria graminis* on excised barley leaves, which was feasible when symptoms became visible on the RGB images at 4 dai. These researchers further improved the monitoring results for visualizing the plant–pathogen interactions at 2 dai, based on SiVM and clustering analysis, 3 days earlier than the visual inspection of corresponding RGB images [30]. However, pathogen inoculation on excised leaves might not represent the pathogenesis on *in vivo* leaves [29,30]. In addition, as SiVM represents the pixel spectrum as a combination of a few extreme signatures, the spectral mixing problem was solved for the subsequent LLRs calculation [29] or clustering analysis [30], but unique fingerprint spectral signatures (FSSs) characterizing the lesions were not extracted. FSSs are unique and representative spectral signatures that characterize a specific plant disease. In a study of the early *in situ* monitoring of *Magnaporthe oryzae*-infected barley leaves using HSI, the lesions were visualized as early as 24 hours after inoculation (hai) by means of spectral unmixing analysis [31]. However, the spectral unmixing analysis was conducted separately on hyperspectral images acquired at 0, 24, 48, and 72 hai. The extracted endmembers differed among all measurement times, and no robust and representative FSSs that could capture the diseased lesions across different times were extracted.

Important advances have been made in the characterization of early spatiotemporal dynamics at the leaf scale for presymptomatic disease diagnosis [13,29–31]. However, no representative and robust FSSs with definite physical interpretations have been extracted to capture lesions across different infection time points on *in vivo* leaves, which could result in reduced robustness and applicability of spectral diagnosis. Moreover, the detection mechanism of HSI via an association with the early host biochemical responses to pathogen infestation has not been investigated in the abovementioned literature, which might lead to poor physical interpretation. In addition, the timeliness of these visualization results was compared with that of the visual inspection, which was inaccurate and hysteretic considering the invisible symptoms in the initial phase and the subjectivity of human observation.

In the present study, leaf-scale hyperspectral images of *in vivo* barley leaves under spot blotch stress were regularly scanned (at

0, 24, 36, 48, 60, and 72 hai), and the FSSs of lesions were extracted for presymptomatic disease diagnosis. The specific objectives of this study were to ① explore the early time-series spectral responses of *in vivo* barley leaves to spot blotch progression and establish a rapid, non-destructive, *in situ* diagnosis methodology for presymptomatic disease based on HSI; ② extract representative, robust, and interpretable FSSs to capture lesions across the early stage of pathogen infection and monitor the spatiotemporal dynamic alterations of early lesion progression *in situ* at the pixel level for the presymptomatic diagnosis of spot blotch; and ③ reveal the mechanism of HSI presymptomatic diagnosis of spot blotch by establishing the mathematical relationships between the spectral characteristics and the host biochemical indicators.

2. Materials and methods

2.1. Plant cultivation and sample preparation

Barley plants (*Hordeum vulgare* L.) were selected as the experimental samples. Seeds were grown in a greenhouse with a 12 h/12 h (day/night) photoperiod at 25 °C, 60% relative humidity for 8 d. Spot blotch pathogen *B. sorokiniana* was grown at 25 °C in potato glucose agar medium for 1 week. The conidial suspension (7.0×10^5 spores·mL^{-1}) was taken and sprayed onto the primary barley leaves (with an approximate length of 10 cm at the eighth day); then, the leaves were covered with transparent covers to maintain the pathogenic environment at a temperature of 25 °C and high humidity of 90%. Two sets of samples (with one leaf per sample) were prepared. The first sample set consisted of 18 infected and five healthy barley leaves, cultivated alive throughout the whole data collection process. To track the infection progression, hyperspectral images of *in vivo* infected and healthy leaves were acquired at 0, 24, 36, 48, 60, and 72 hai, respectively, resulting in 138 images altogether. Another sample set went through the same pathogen inoculation treatment, but these samples were excised from the plant to be used for the destructive measurement of leaf biochemical indicators at the same time points as the first sample set. A total of 250 samples were collected and divided equally into two sets: One set was for pigment measurement, including chlorophyll a (Chl-a), chlorophyll b (Chl-b), and carotenoids (Car); the other set was for the measurement of oxidative- and antioxidative-related compounds (MDA, AsA, and GSH). Detailed information for the prepared samples is presented in Table 1. Photosynthetic pigments (chlorophylls and Car) were selected since they are sensitive to pathogen infection associated with the occurrence of necrotic or chlorotic lesions [11]. MDA was included because it is frequently taken as an indicator of peroxidation of membrane lipids due to the excessive ROS produced under disease stress [17,18]. AsA and GSH, which act as important antioxidants in the defense against ROS attack [17], were also studied.

2.2. Acquisition of hyperspectral images

To acquire hyperspectral images, a line-scanning HSI system (380–1030 nm) was used, consisting of an ImSpector V10E imaging spectrometer (Spectral Imaging Ltd., Finland) with a high spectral resolution (2.8 nm), a C8484-05G charge-coupled device (CCD) camera (Hamamatsu Photonics K.K., Japan) with 1.37 megapixels, an IRCP0076 conveyor belt (Isuzu Optics Corp., China), and two 150 W line 9596ER tungsten halogen lamps (Illumination Technologies Inc., USA). Leaf samples were put on a blackboard with low reflectivity, with the leaf base and tip fixed with tape to reduce the influence of surface unevenness. Samples were immediately put back into the moistened chamber after each HSI scan with uniform acquisition parameters. The image resolution was set to 1024×472, the exposure time was 0.06 s, the distance between samples and the lens was 270 mm, and the moving speed of the conveyor belt was 3.0 mm·s^{-1}. All raw hyperspectral images were corrected with white and dark reference images [32] before further analysis.

2.3. Measurement of leaf biochemical indicators

Healthy and infected barley leaf samples collected at 0, 24, 36, 48, 60, and 72 hai were weighed and put into liquid nitrogen for rapid cooling to prepare for downstream chemical measurements. The contents of the six biochemical indicators were measured using a microplate spectrophotometer (Epoch 2; Biotek, USA). To measure Chl-a, Chl-b, and Car, the sample was extracted with 95% ethanol at 4 °C without light, followed by absorbance measurement at 665, 649, and 470 nm for concentration calculation [33]. Because AsA can reduce ferric ions (Fe^{3+}) to ferrous ions (Fe^{2+}), a solution of Fe^{3+} was added to the sample, and bipyridine was added to the resulting Fe^{2+} to form a red chelate. The absorbance was then measured at 525 nm to determine AsA concentration [34]. To calculate GSH concentration, GSH was reacted with 2-nitrobenzoic acid (DTNB) to form yellow 2-nitro-5-mercaptobenzoic acid, and the absorbance at 412 nm was measured [34]. To calculate MDA concentration, MDA was reacted with thiobarbituric acid (TBA) under acid conditions to form a red–brown trimethyl complex (3,5,5-trimethyloxazole-2,4-dione), and the absorbance at 532 nm was measured [35].

2.4. Quantification of fungal infection degree in barley leaves via real-time PCR

2.4.1. Design of specific primers

The ratio of fungus to plant DNA (fungus/plant DNA ratio, FPDR) was used to monitor the degree of fungal infection in barley leaves. It was determined by means of the $2^{-\Delta C_t}$ method [36], where ΔC_t is the difference between the raw cycle threshold values (C_t) of the *B. sorokiniana tef-1α* gene and the barley *Ubiquitin* gene [37,38]. Specific primers were designed based on *B. sorokiniana tef-1α*. This gene was partially amplified with the primers EF728 and EF986 (Table S1 in Appendix A) using the following profile: 94 °C for 3 min, followed by 35 cycles of 94 °C for 30 s, 52 °C for 30 s, and 72 °C for 30 s, with a final extension at 72 °C for 10 min. The amplified product was then sequenced. The specific primer set BM-F/BM-R (Table S1) was designed to amplify a region of 136 bp.

Table 1
Sample set for the measurement of the biochemical indicators of barley leaves over the infection time.

Time (hai)	Chl-a, Chl-b, and Car		MDA, AsA, and GSH	
	Infected group	Healthy group	Infected group	Healthy group
0	—	15	—	15
24	16	5	16	5
36	18	5	18	5
48	18	5	18	5
60	17	5	18	5
72	16	5	15	5

2.4.2. Genomic extraction and real-time PCR

B. sorokiniana-inoculated leaves were harvested at 0, 12, 24, 36, 48, 60, and 72 hai. The disease area was collected and ground in liquid nitrogen for DNA extraction using a Plant DNeasy Kit (Qiagen, Germany). For real-time PCR, 50 ng of total DNA was amplified in a total volume of 20 μL containing 10 μL of 2× SYBR Premix Ex Taq (Takara Bio Inc., Japan) and 1 μL of 10 μmol·L^{-1} BM-F/BM-R primers (or *Hv*Ubiq-F/R for the barley *Ubiquitin* gene) on a Mastercycler ep realplex Thermal Cycler (Eppendorf, USA). A melting curve analysis was added to ensure that only one single product was obtained. Each reaction was performed in triplicate.

2.5. Data analysis

The systematic framework diagram of this study is shown in Fig. 1. After sample preparation and the acquisition of hyperspectral images, the biochemical indicators and FPDR were measured and taken for statistical analysis. Next, hypercube pixel-wise visualization algorithms were conducted, in which the spectral unmixing analysis achieved accurate infection identification and extracted the FSSs of the lesions. The application of FSSs on the time-series hyperspectral images realized lesion tracking on *in vivo* leaves, enabling the presymptomatic diagnosis of spot blotch. Finally, the quantitative relationships between the spectral features of the leaves and their biochemical indicators under spot blotch stress were established to reveal the mechanism of HSI presymptomatic diagnosis.

2.5.1. Lesion visualization on two dimensional (2D) hyperspectral images

To identify the diseased sites of spot blotch and intuitively visualize the infection processes, several pixel-wise methods including *k*-means clustering, fuzzy clustering, and the spectral unmixing method, were adopted. *k*-means is an iteratively updated unsupervised clustering algorithm [39]; herein, the given number of clusters was set as 4. For fuzzy clustering analysis, the fuzzy c-means algorithm (FCM) was chosen, which calculated a weight to each pixel, representing its membership degree relative to different categories [40]. The number of categories of FCM was also set as 4. The spectral unmixing method, which originates from the field of remote sensing, is one of the most important methods of spectral information mining; it was used to solve the problem of extracting specific component information from the mixed spectrum. Spectral unmixing included decomposing a mixed spectrum into several

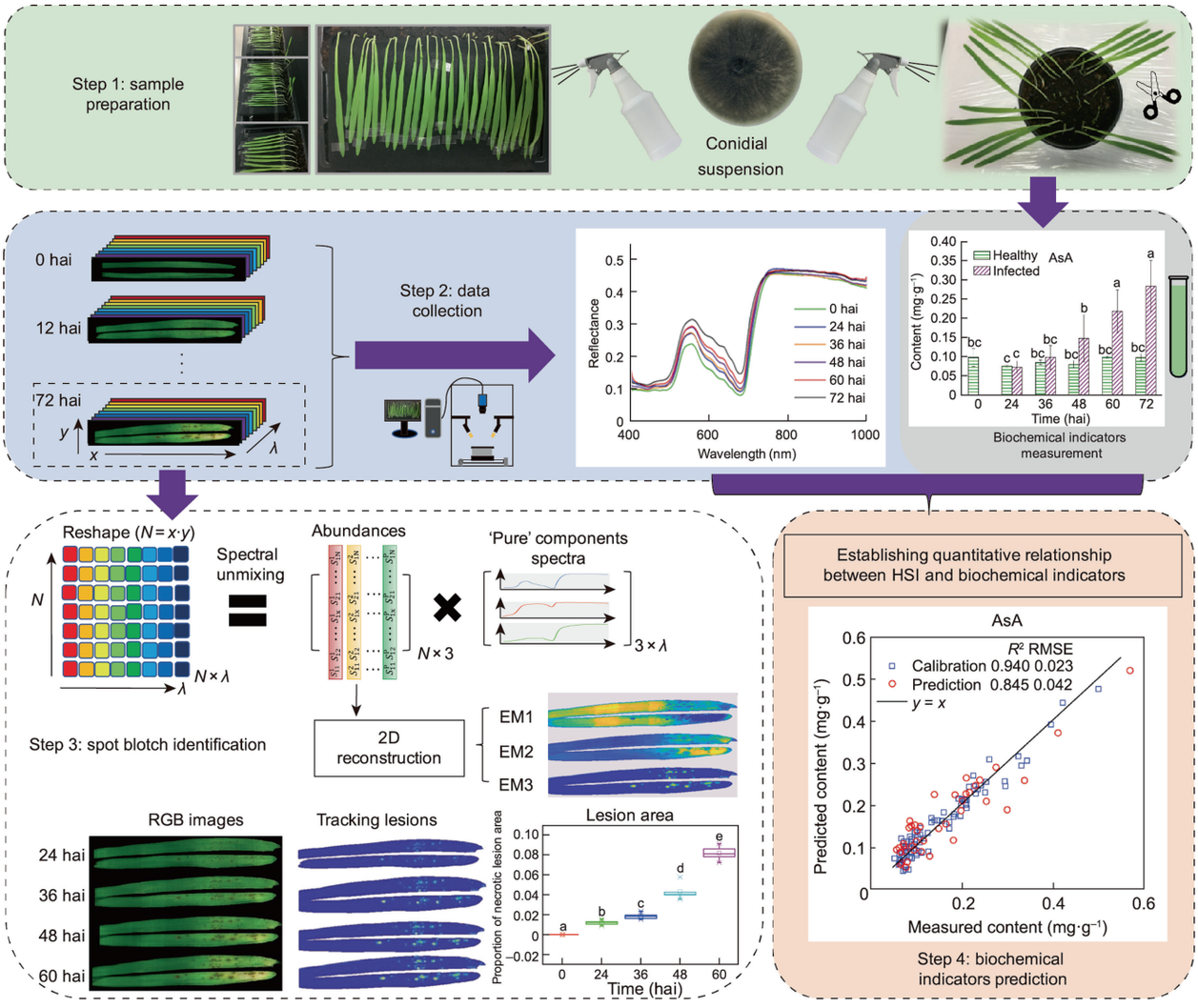

Fig. 1. The systematic framework diagram of this study. 2D: two dimensional; R^2: determination coefficient; RMSE: root mean square error; EM: endmember; *S*: the abundance value of each pixel spectrum. Different letters (a, b, c, d, and e) are used to represent significance at $p < 0.05$.

component spectra (endmembers, EMs) and estimating the spatial distributions (abundances) of each EM. The index of abundance represented the proportion of each EM in a single pixel [41]. Vertex component analysis (VCA), as an unsupervised approach, was applied to extract the EMs based on the convex geometry theory and to calculate the abundances for each pixel spectrum by means of non-negative constrained least squares [42].

2.5.2. Data compression, modeling, and characteristic wavelengths selection on one dimensional (1D) spectra

For each leaf sample, the mean spectrum was extracted to study the averaged spectral response of the barley to spot blotch infection. To visualize the overall distribution of spectral characteristics, data dimensionality reduction was executed using PCA, which yielded the orthogonal principal components (PCs) through the conversion of original variables while preserving most of the information [43].

To establish the effective mathematical relationship between the spectral responses and the biochemical indicators, the Monte Carlo partial least squares (MCPLS) method was first used to eliminate abnormal samples for each indicator [44]. After random sample partitioning into calibration and prediction sets with a 2:1 ratio, partial least squares (PLS) regression for full-spectrum modeling was conducted with a total of 392 wavelengths of 450–950 nm. PLS is a classical multivariate modeling method, which transforms the original spectra linearly to obtain orthogonal latent variables (LVs). In addition, to identify the most representative and interpretable wavelengths while minimizing the redundancy among adjacent spectral bands, characteristic wavelengths were selected by four variable selection methods, including iterative random frog (RF), competitive adaptive reweighted sampling (CARS), successive projections algorithm (SPA), and stepwise regression [45]. Simplified models were then constructed by means of multiple linear regression (MLR).

2.5.3. Software and model evaluation

The hyperspectral images were masked to remove the background using ENVI software (ITT Visual Information Solutions, USA). The analysis of variance (ANOVA), spectral smoothing, regression analysis, characteristic wavelengths selection, and lesion visualization were all conducted using the MATLAB software (The Math Works, Inc., USA). The performances of the regression models were evaluated by means of the determination coefficient (R^2), root mean square error (RMSE), and residual predictive deviation (RPD) of the calibration and prediction sets. Models with good performance should have high R^2 and RPD values and low RMSE values. The leaf lesion visualization performance was evaluated by comparisons with RGB images and by mutual comparison among different infection time points.

3. Results

3.1. Degree of pathogen infestation according to real-time PCR over time

The FPDR index is widely used to evaluate the degree of fungal pathogen infection in plants. The time-series FPDR measurement results (Fig. 2) revealed an early steady state within 24 hai, without significant differences among the samples at 0, 12, and 24 hai. Subsequently, the pathogen biomass increased significantly at 36 hai, which was the first time point that manifested significant growth in the degree of infection. Following a moderate increase at 60 hai, a final remarkable increase at 72 hai occurred. In addition, the pathogen showed a trend of unlimited proliferation in the leaves without plant control, which aggravated the diseased lesions and killed the host plant.

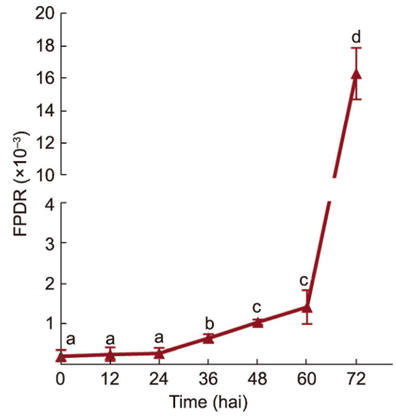

Fig. 2. Fungal colonization curve plotted with means ± standard deviation (SD) of three replicates using real-time PCR on barley leaves over infection time. Different letters (a, b, c, and d) are used to represent significance at $p < 0.05$.

3.2. Responses of leaf biochemical indicators to spot blotch infection over time

A correlation analysis between the biochemical indicators and the PCR data (Fig. 3) revealed that Chl-a, Chl-b, Car, GSH, and MDA were significantly correlated with the PCR data, indicating that the fungal infection caused substantial changes in the biochemical indicators of the barley leaves. To display the detailed changes in these indicators for all samples over the infection time, an ANOVA was conducted, as shown in Fig. 4 and Table S2 in Appendix A. The fungal infection induced significant differences between the healthy and infected barley leaves for all indicators, and these significant changes became more apparent over the infection time. Table S2 shows the significant effect of infection time on these six indicators, with p values below 0.01. The most sensitive indicators were Chl-a and Chl-b, which showed a significant difference between the healthy and infected samples from 36 hai. This significant difference later appeared in Car, AsA, GSH, and MDA at 60, 60, 48, and 48 hai, respectively.

3.3. Responses of leaf spectral characteristics to spot blotch infection over time

Responses of the spectral characteristics of barley leaves to spot blotch infection over time are shown in Fig. 5. The spectra of typical infected pixels at 0, 24, 36, 48, 60, and 72 hai are shown in Fig. 5(b). The mean spectra with standard deviation of the infected and healthy groups at different time points (24, 36, 48, 60, and 72 hai) were calculated, as shown in Fig. 5(d). An ANOVA between the healthy and infected groups at different time points (Fig. 5(d)) revealed that the first significant spectral difference between the two groups appeared at 36 hai at 545–680 nm, when the fungal biomass showed a significant increment (Fig. 2). The higher reflectance in this spectral range of the infected leaves was mainly due to the weakened absorption of red light by the reduced chlorophyll in the barley leaves under spot blotch stress, which was validated by the reduced Chl-a and Chl-b contents in the infected leaves from 36 hai (Fig. 4). In accordance with the increased significant differences between the healthy and infected groups in the biochemical indicators over the infection time, the spectral differences between the two groups also gradually increased (Figs. 5 (b) and (d)), which was associated with the typical spot blotch pathogenesis on *in vivo*

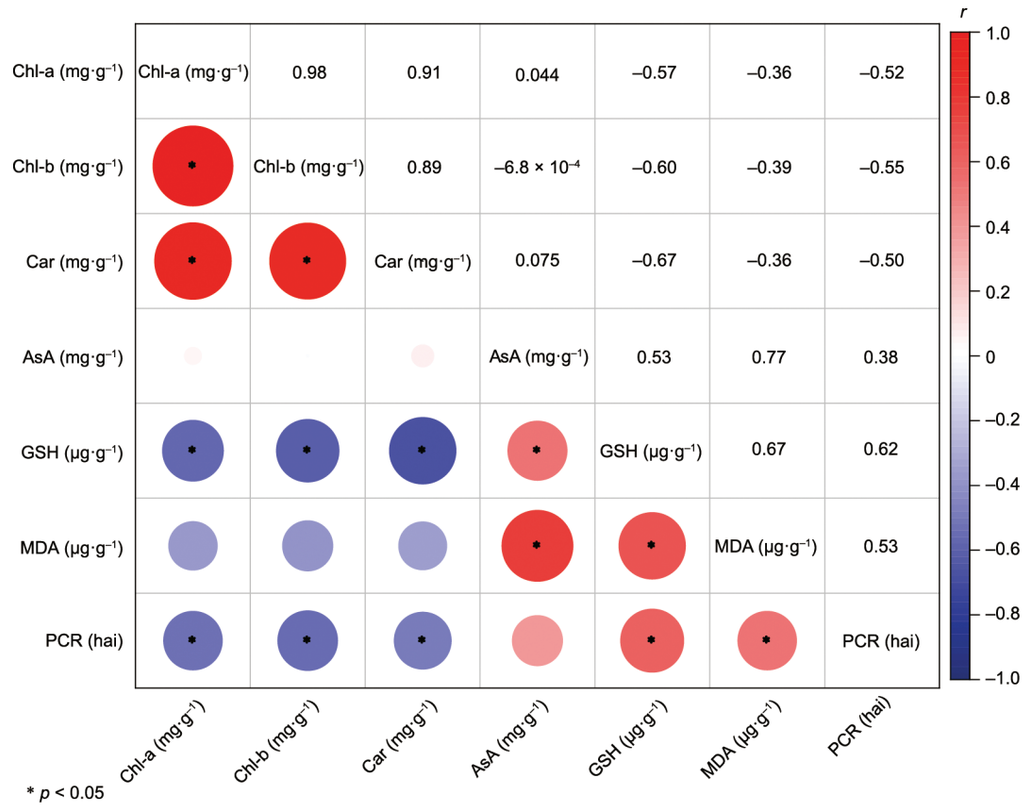

Fig. 3. Correlation analysis of biochemical indicators and PCR data of barley leaves under spot blotch stress. *r*: correlation coefficient.

barley leaves. The significant spectral difference became more prominent at 72 hai, spanning the spectral range of 455–735 nm (Fig. 5(d)). As the disease progressed, the standard deviation of the mean spectra of the infected samples displayed an increasing trend, indicating increased heterogeneity in the internal structure and composition of the leaves as their intercellular space was penetrated by the fungus [46]. This spatial heterogeneity in the infected tissue is depicted in Fig. 5(c), which shows the spectra of a certain line in the infected area at 72 hai. The apparent spectral differences between the healthy and infected samples at different time points are also shown in Fig. S1 in Appendix A, which displays the distribution of the first three PCs after PCA on the extracted mean spectra.

The above spectral observations confirmed the usefulness and convenience of the averaged spectral profiles of HSI for reflecting the general physiological and biochemical alterations in plants during pathogenesis [10,16,20]. However, due to the use of mean values, the advantages of imaging spectroscopy were not fully exploited [13,21]. Pathogen-induced stress usually manifests as small and scattered areas around the initial infection sites on leaves. Therefore, it was necessary to integrate the image information of HSI in order to consider the spatial heterogeneity of infected leaves in the subsequent analysis.

3.4. Lesion visualization by k-means clustering and FCM

Lesion visualization by means of clustering analysis on a barley leaf infected with spot blotch is shown in Fig. 6. The leaf hyperspectral image at 60 hai was selected to compare the performances of the different pixel-wise analysis methods. Clustering algorithms have been demonstrated to distinguish infection information from high-dimensional data [47]. The results of *k*-means clustering are shown in Fig. 6(b). *k*-means clustering was able to identify the chlorotic regions colored in light blue near the leaf tip; however, the important dark brown lesions could not be identified. The leaf edges were grouped into a new category (marked in blue), which did not align with the actual spatial distribution characteristics of the leaf spectra. As *k*-means clustering functions as an unsupervised hard clustering algorithm, one pixel could only be assigned to one category, which could not satisfy the monitoring of complex and mixed signal features on the plant–pathogen interaction sites.

The calculated representative spectra of the four categories and their corresponding membership degree maps from the FCM analysis are shown in Figs. 6(c) and (d), respectively. The representative spectra of category 1 (C1) represent the chlorotic region, and the C1 membership map shows the distribution of chlorotic regions on the leaf. Category 4 (C4), which has a low spectral reflectance, represents the leaf edge. For C2 and C3, although some infected regions can be detected in their membership degree maps, some healthy tissues have been misclassified as infected. Thus, FCM was also unable to identify necrotic lesions, which might be due to its inability to consider any information about spatial context and sensitivity to image noise [48].

3.5. Lesion visualization and FSSs extraction by means of VCA

As the above clustering methods failed to effectively identify spot blotch lesions, the spectral unmixing method of VCA was employed (Fig. 7). Three representative spectra (EMs) were extracted from the hyperspectral image, and their corresponding abundance maps were generated, as shown in Figs. 7(b) and (c), respectively. It should be noted that the extracted EMs can be assigned to different categories associated with prior knowledge, relative to the data. In Fig. 7(b), the EM1 spectral profile appears

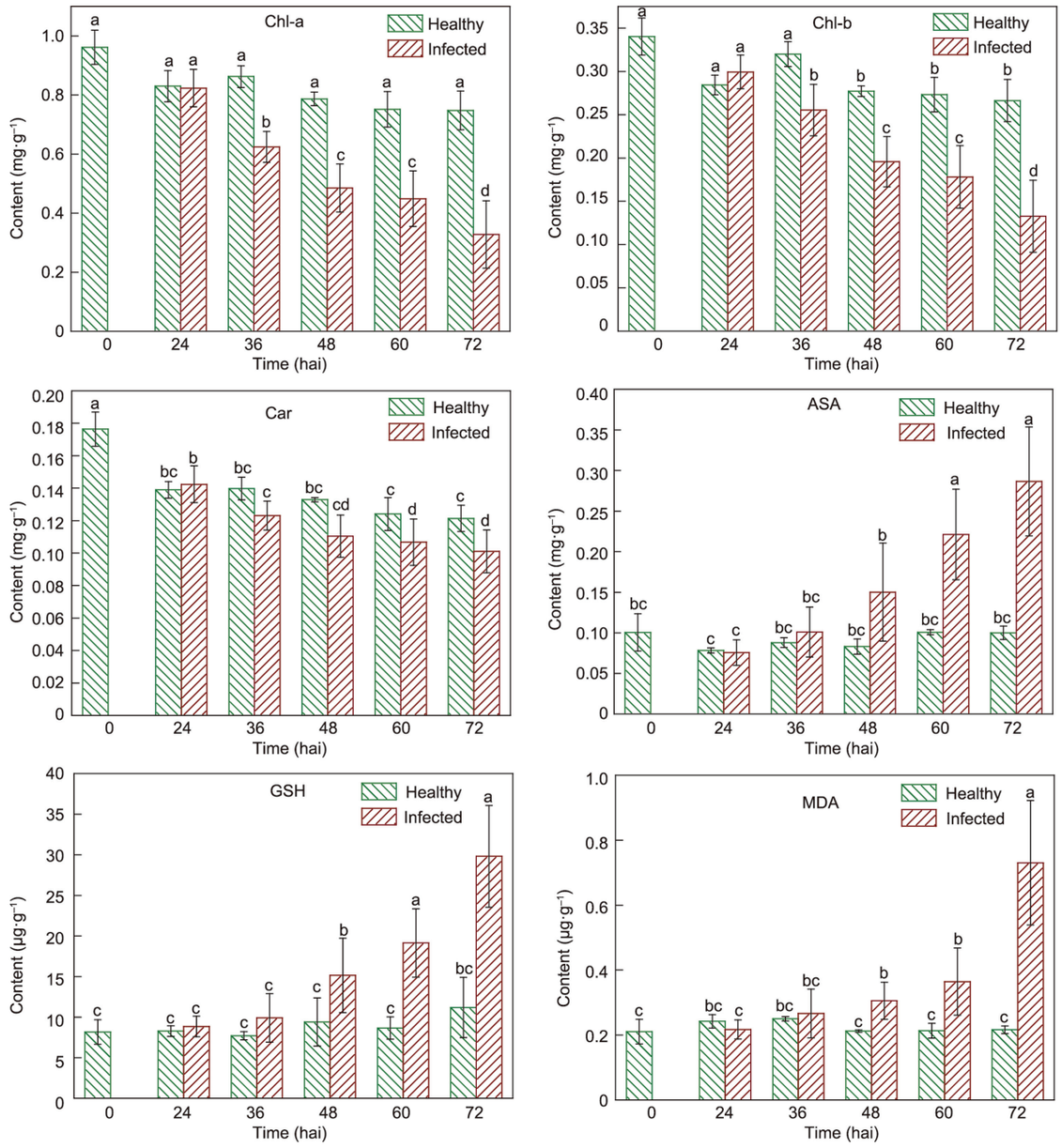

Fig. 4. Responses of biochemical indicators of barley leaves to spot blotch infection over time. Different letters (a, b, c, and d) are used to represent significance at $p < 0.05$.

as an obvious reflection peak from 450 to 650 nm, especially in the visible green light region, with an abrupt increase in reflectance at the red-edge inflection position in the 680–750 nm region and high reflectance in the near-infrared region, indicating strong chlorophyll absorption and healthy internal scattering within mesophyll tissues [20,29,49]. The abundance map of EM1 in Fig. 7(c) aligns with the distribution of healthy leaf tissues in Fig. 7(a) (the RGB image), confirming that the EM1 can be attributed to the FSS of healthy leaf tissue.

The abundance map of EM2 in Fig. 7(c) highlights the chlorotic regions in the infected leaf in the RGB image (Fig. 7(a)). The EM2 spectral profile (Fig. 7(b)) loses the typical reflection peak in the visible green light region, which is replaced by a relatively flat reflex plateau with high reflectance (low absorbance). The red-edge effect is also significantly weakened, indicating considerable destruction of the chlorophylls in the mesophyll. The reflectance intensity of the EM2 spectral profile in the near-infrared region declines moderately compared with that of EM1, indicating that the dense and organic structure of the chlorotic mesophyll tissue has been damaged to some extent [20,49]. Hence, EM2 is attributed to the FSS of the slightly infected tissues with signs of chlorosis. Compared with the membership degree map 1 obtained via FCM in Fig. 6(d), the spatial differentiation for the chlorotic region based on the VCA method is more accurate.

The abundance map of EM3 accurately captures the location of dark brown necrotic lesions, as shown in Fig. 7(c); even the small granular lesions are clearly discernable. The EM3 spectral profile (Fig. 7(b)) displays an intriguing and unique FSS of necrotic lesions. Compared with the FSS of healthy (EM1) and chlorotic (EM2) tissues, a slow ascent process with a small slope appears from 450 to 550 nm. It is notable that the typical healthy leaf reflection peak in the range of 550–650 nm is almost cut flat with

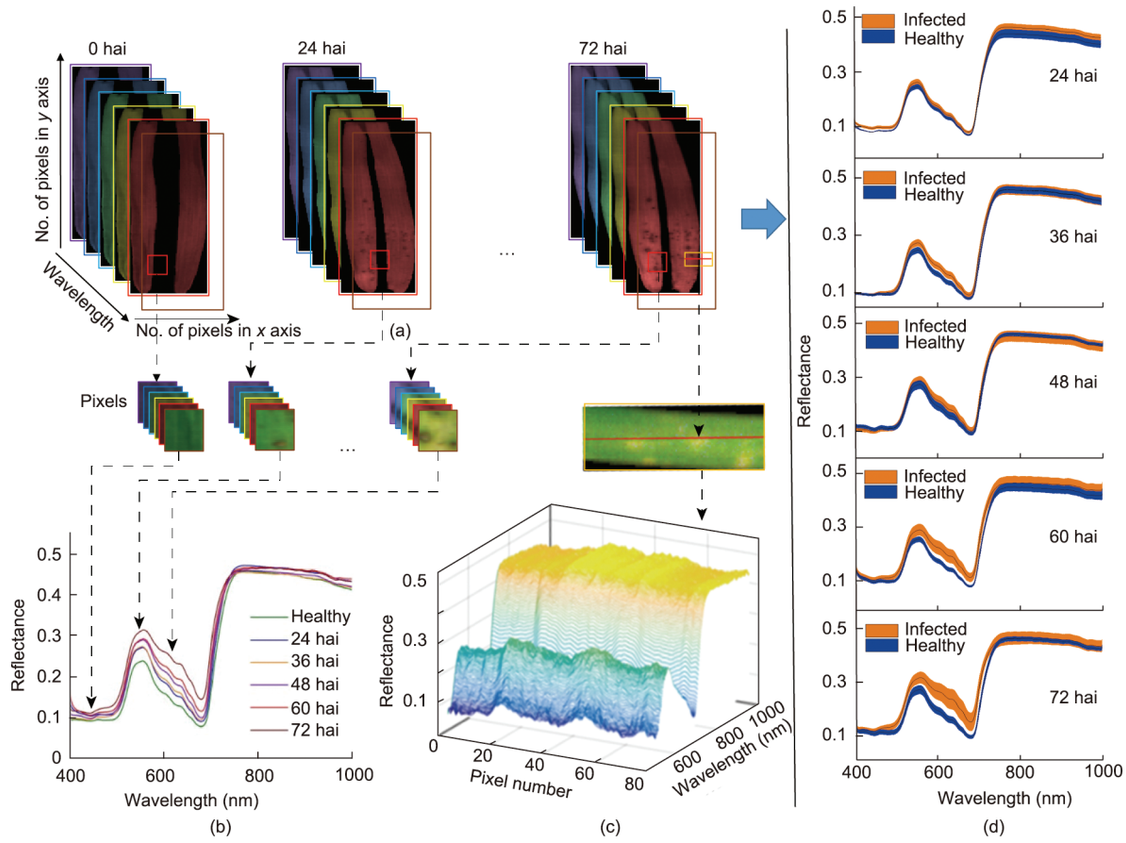

Fig. 5. Responses of the spectral characteristics of barley leaves to spot blotch infection over time. No.: number.

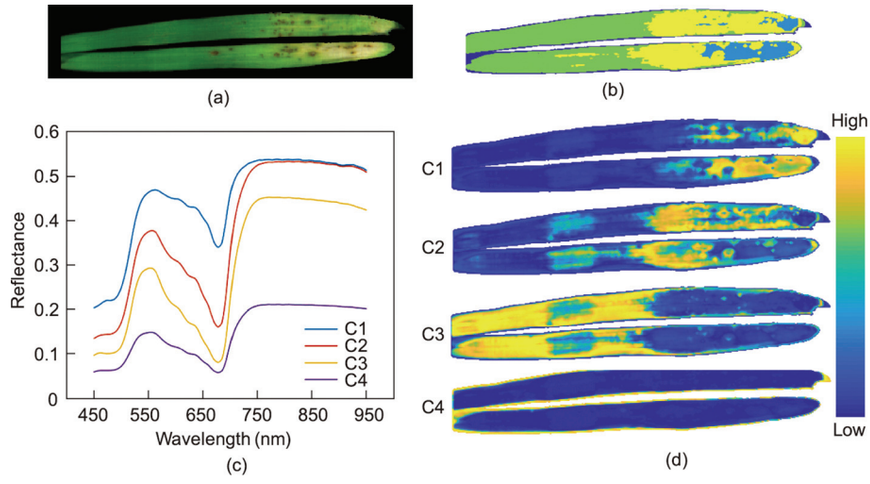

Fig. 6. Lesion visualization by means of clustering analysis on a barley leaf infected with spot blotch. (a) RGB image; (b) results of *k*-means clustering; (c) calculated spectral signatures of four categories and (d) their corresponding membership degree maps using FCM. C1–4: category 1–4.

very low reflectance, due to the strong light absorption by the darkened lesion tissues (shown in the RGB image of Fig. 7(a)), and the serious degradation of the pigments (referring to the declined pigment concentrations at later infection times in Fig. 4). The typical red-edge spectral feature of healthy tissues is replaced with arc-shaped reflection lines from 680 to 950 nm, with obviously reduced curvature in the EM3 spectral profile (Fig. 7(b)), which is a typical trait of necrotic lesions. The substantially reduced reflectance in the near-infrared range of 780–950 nm indicates the complete destruction of the dense ordered structure inside these lesion tissues [20,49]. To validate the structural properties of the three types of mesophyll tissues (healthy, slightly infected with chlorosis, and heavily infected with necrosis) reflected by the FSSs in the near-infrared range, microscopic images of the transverse sections of these leaf tissues are shown in Fig. 8.

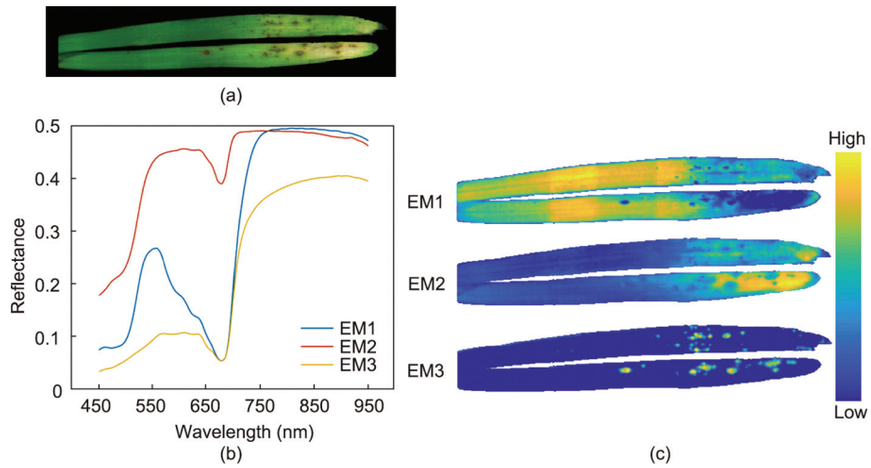

Fig. 7. Lesion visualization by VCA on a barley leaf infected with spot blotch. (a) RGB image; (b) EM1–3 spectral profiles denoting the FSS of healthy, chlorotic lesion, and necrotic lesion tissues, respectively; (c) abundance maps of EM1–3.

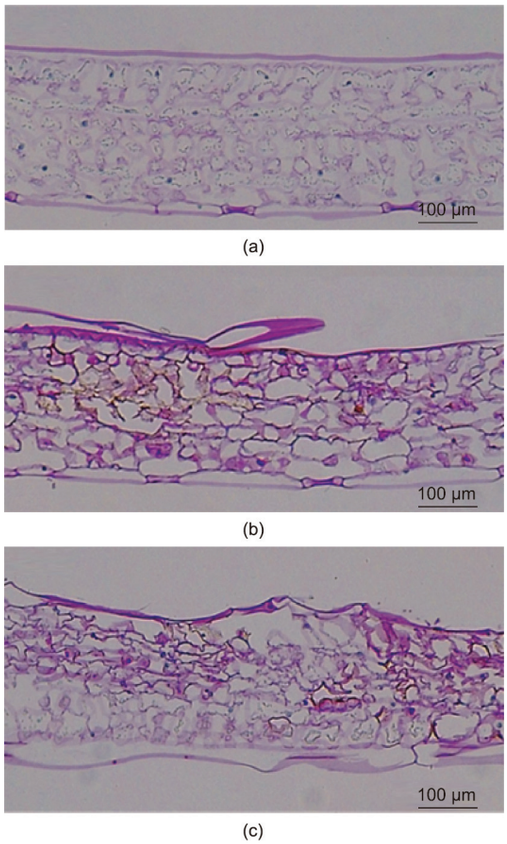

Fig. 8. Microscopic images of stained sections corresponding to (a) healthy tissue, (b) slightly infected chlorotic lesion tissue, and (c) heavily infected necrotic lesion tissue of barley leaves under spot blotch stress.

The healthy tissue in Fig. 8(a) shows the typical leaf structure of barley, with compactly arranged layers of epidermis, palisade, and spongy mesophyll cells. The structure of the slightly infected chlorotic tissue in Fig. 8(b) maintains its overall integrity, with intact epidermal layers and stomata cells. However, the local physical structure within the mesophyll has collapsed with the rupture of spongy cells due to the cell-to-cell spreading of invasion hyphae via the penetration of the barriers among cells. The partial destruction of the internal structure in the chlorotic region of the barley leaf corresponds to the moderately declined reflectance of the EM2 spectral profile in the near-infrared region (Fig. 7 (b)). In the severely infected necrotic tissue shown in Fig. 8(c), the cells are collapsed or deformed through all layers of the leaf. The upper epidermal layer is completely destroyed where a cavity has formed, which might be due to the encroachment of conidiophores that escaped during leaf staining. The lower epidermis has been loosened, with damage to the stomata. The palisade and spongy mesophyll cells are occupied by penetrated hyphae, with an increase in electrolyte leakage and fungal toxin infiltration [1]. The complete structural destruction in the necrotic lesion on the barley leaf corresponds to the evidently reduced reflectance of the EM3 spectral profile in the near-infrared region in Fig. 7(b). The structural properties of the three types of mesophyll tissues in the above microscopic observations are highly consistent with those reflected by the FSSs responses in the near-infrared range. Thus, the FSSs extracted by the spectral unmixing analysis of VCA can achieve definite physical interpretation of the original HSI data. Moreover, the increased spatial heterogeneity in the leaf structure due to the fungal invasion, as observed from the microscopic images, validates the enlarged variance of the mean spectra along with disease progression (Fig. 5).

3.6. Visualization of lesion spatiotemporal dynamics via the extracted FSSs for presymptomatic diagnosis

Lesion visualizations based on calculations of the spatial distributions of FSSs at 24, 36, 48, and 60 hai are shown in Fig. 9. The occurrence and progression of spot blotch on barley leaves can be tracked through the abundance maps, with healthy, chlorotic lesion, and necrotic lesion regions clearly separated (the two broad yellow strips in the middle of the leaves in Fig. 9(b) are caused by the tape that was used to keep the leaf flattened during HSI scanning). Fig. 9 shows that, with a prolongation of the infection time from 24 to 60 hai, the continuous and subtle changing pattern of disease symptoms can be conspicuously visualized with the gradual diminution of the healthy region and the increment of chlorotic and necrotic lesion regions. Evidently, as early as 24 hai, tiny lesions invisible to the naked eye are captured by the hybrid of HSI and FSSs, as shown in Figs. 9(c) and (d).

The proportion of necrotic lesion area was calculated and plotted against the infection time, as shown in Fig. 10. Necrotic lesion

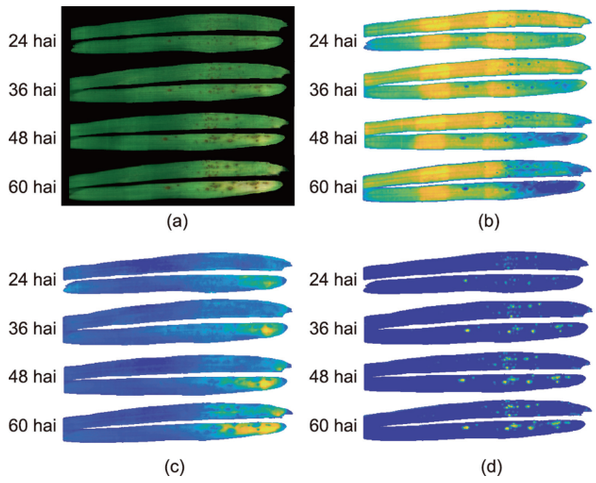

Fig. 9. Lesion visualization by the extracted FSSs over time for the presymptomatic diagnosis of spot blotch on barley leaves. (a) RGB; (b) healthy region; (c) chlorotic lesion region; (d) necrotic lesion region.

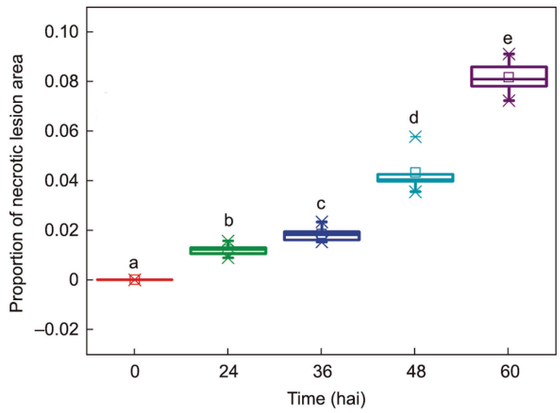

Fig. 10. Box plot of the proportion of necrotic lesions on the area of the barley leaves over the infection time. Different letters (a, b, c, d, and e) are used to represent significance at $p < 0.05$.

spots appear at 24 hai, followed by exponential expansion over the infection time. Moreover, the areas of necrotic lesions tracked by our method at 0 hai and 24 hai are significantly different ($p = 0.008$). However, neither traditional PCR (Fig. 2) nor a biochemical analysis (Fig. 4) detected significant differences in the diagnosis of leaf disease symptoms at 24 hai, indicating that our proposed method achieves the ultra-early diagnosis and location of spot blotch lesions.

3.7. Relationship between spectral responses and biochemical indicators under spot blotch stress

To reveal the mechanism of the HSI presymptomatic diagnosis of spot blotch, quantitative relationships between the averaged spectral responses and their corresponding biochemical indicators were explored. The performances of the full-spectrum PLS regression models are presented in Table 2. All models achieved good prediction results ($R_p^2 > 0.720$), especially for chlorophylls and Car, with $R_p^2 > 0.870$, indicating that the spectral characteristics of HSI can quantitatively determine the biochemical properties of barley leaves under pathogen stress. Improved quantification results were achieved using the MLR models based on the characteristic wavelengths selected by CARS or RF, as shown in Table S3 in Appendix A. The optimal characteristic wavelengths were identified (Fig. S2 in Appendix A) for assignment analysis (Table S4 in Appendix A) according to the literature [32,49–51], and the six final MLR models were then constructed, with $R_p^2 > 0.84$ (scatter plots shown in Fig. S3 in Appendix A).

3.8. Test of VCA on other plant diseases

To test the generalization and transferability of the VCA method to other plant–pathogen systems, eggplant leaf infected with early blight disease and cucumber leaf infected with angular leaf spot disease were taken for analysis. The lesion visualization results are shown in Figs. 11 and 12, respectively. It can be seen that the disease on the eggplant leaf is in the early infection stage, while the cucumber leaf disease is in the medium infection stage. Through the VCA spectral unmixing analysis, each pixel spectrum on the eggplant leaf was decomposed into three EMs representing the FSSs of the leaf vein, healthy, and lesion tissues, respectively, while each pixel spectrum on the cucumber leaf was decomposed into three EMs representing the FSSs of healthy, slight-chlorotic lesion, and yellowish-brown lesion tissues, respectively. The infected lesion regions in the EM3 abundance map of the eggplant leaf, as well as those in the EM2 and EM3 abundance maps of the cucumber leaf, were more pronounced than those in the corresponding RGB images. The application of these FSSs to hyperspectral images of early-infected presymptomatic eggplant and cucumber leaves could achieve similar detection results as the ultra-early diagnosis of spot blotch on barley leaves.

4. Discussion

4.1. Fungal infestation and biochemical responses of barley leaves

The developmental process of *B. sorokiniana* infection in barley leaves displays an increasing trend in the FPDR (Fig. 2). According to the literature [2–4], initial infection with *B. sorokiniana* starts with conidia germination on the leaf (within 4 hai), formation of the appressorium (8 hai), and penetration of hyphae into the leaf cuticle (12 hai), followed by the spread of hyphae from initially infected cells to adjacent cells at 24 hai. The initial fungal colonization process explains the slow increase in the FPDR from 0 to 24 hai. Thereafter, the fungus invades the plant tissue via rapid division of infection hyphae to ramify along the intercellular spaces of the mesophyll tissue and produce conidiophores [3]. Under optimal conditions, the hyphae produce conidiophores that merge out through the leaf stomata and produce a new generation of conidia within 48 hai [2]. Thus, after approximately 60 hai, intensive invasion and colonization within the leaf tissue are to be expected due to the succession of conidia, ultimately explaining the moderate and rapid increase in the FPDR before and after 60 hai, respectively (Fig. 2).

Under the stress of fungal infestation, the early biochemical responses of the barley leaves to spot blotch disease were revealed by changes in the biochemical indicators (Fig. 4). The invasion of *B. sorokiniana* led to the destruction of the mesophyll structure through hyphae spreading and the collapse of mesophyll cells through fungal toxin secretion [1]. Under disease stress, the intracellular oxidative metabolism of the leaves was enhanced, producing high levels of ROS, which further induced a series of biochemical changes at the cellular level [18,52]. The ROS increment and fungal toxin infiltration resulted in damage to the photosynthetic machinery and inhibition of photosynthesis [1,17], which manifested as the continuous decomposition of photosynthetic pigments, including Chl-a, Chl-b, and Car, over the infection time

Table 2
Results of full-spectrum PLS models for quantifying the biochemical indicators of barley leaves under spot blotch stress.

Biochemical indicator	LV	R_c^2	RMSEC	RPD_c	R_p^2	RMSEP	RPD_p
Chl-a ($mg \cdot g^{-1}$)	6	0.939	0.054	3.568	0.879	0.077	2.972
Chl-b ($mg \cdot g^{-1}$)	12	0.947	0.016	3.677	0.883	0.024	3.173
Car ($mg \cdot g^{-1}$)	13	0.918	0.008	3.320	0.874	0.010	2.904
AsA ($mg \cdot g^{-1}$)	10	0.863	0.034	2.782	0.729	0.055	1.889
GSH ($\mu g \cdot g^{-1}$)	9	0.847	3.769	2.653	0.841	4.098	2.635
MDA ($\mu g \cdot g^{-1}$)	11	0.888	0.068	3.179	0.754	0.101	2.001

LV: latent variable; R_c^2: determination coefficient of the calibration set; RMSEC: root mean square error of the calibration set; RPD_c: residual predictive deviation of the calibration set; R_p^2: determination coefficient of the prediction set; RMSEP: root mean square error of the prediction set; RPD_p: residual predictive deviation of the prediction set.

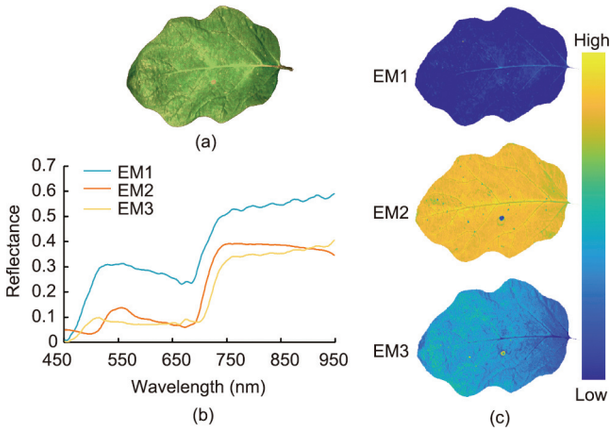

Fig. 11. Lesion visualization by means of VCA on an eggplant leaf infected with early blight disease. (a) RGB image; (b) EM1–3 spectral profiles denoting the FSSs of leaf vein, healthy, and lesion tissues, respectively; (c) abundance maps of EM1–3.

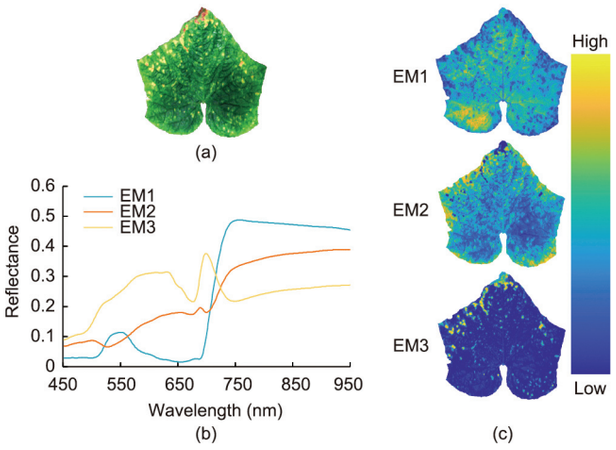

Fig. 12. Lesion visualization by means of VCA on a cucumber leaf infected with angular leaf spot disease. (a) RGB image; (b) EM1–3 spectral profiles denoting the FSSs of healthy, slight-chlorotic lesion, and yellowish-brown lesion tissues, respectively; (c) abundance maps of EM1–3.

(Fig. 4). Previous studies also validated the significant decreases in chlorophylls and Car in diseased leaves at the early stage [11,46]. The retarded reduction of Car in infected leaves compared with the sensitive decline in chlorophylls (a significant difference appeared at 60 vs 36 hai) might be due to the photo-protection function of Car from oxidative damage [17].

Excessive ROS accumulation within cells led to the peroxidation of membrane lipids, resulting in an increase in MDA concentrations [17,18], as shown in Fig. 4. MDA content has been frequently taken as an indicator of lipid peroxidation and stress-induced cellular damage, positively correlating with both spot blotch severity and lesion size in wheat [53]. The moderate and sharp increase in MDA content in the infected leaves before and after 60 hai, respectively, matched with the increasing pattern of FPDR in the PCR assay (Fig. 2), indicating advanced pathogen infestation after 60 hai. To defend against the damage caused by the high levels of ROS, a series of antioxidant cycles were enhanced in the barley leaves to scavenge excessive ROS, which manifested as the steadily increased synthesis of AsA and GSH as non-enzymatic antioxidants [17] in the infected group (Fig. 4). The earliest time point of biochemical significant difference at 36 hai aligned with that of the PCR assay, indicating the importance of exploring the early metabolic responses of barley leaves to pathogen invasion.

4.2. Visualization of lesion spatiotemporal dynamics by the extracted FSSs for presymptomatic diagnosis

To exploit the high-resolution spectral and spatial information, the hyperspectral images were analyzed in a pixel-wise manner to visualize the plant–pathogen interactions during the early stage of infection. Based on a comparison of the visualization results analyzed by *k*-means clustering, FCM, and VCA, *k*-means clustering failed to divide the boundary between healthy and infected areas, and the FCM method improved the visualization quality of the chlorotic region but could not identify the necrotic lesions of the spot blotch. Only the VCA method successfully identified the infected regions and distinguished slightly infected chlorotic lesions from heavily infected necrotic lesions. Using FSSs extracted by means of VCA on the time-series hyperspectral images (Figs. 9 and 10) made *in situ* visualization of the onset and development of pathogen infection possible, enabling the presymptomatic diagnosis of spot blotch on *in vivo* barley leaves at 24 hai—significantly earlier than the traditional PCR detection method and biochemical measurements at 36 hai, as shown in Figs. 2 and 4, respectively. This result can be attributed to the fine and scattered spatial heterogeneity in the structure and the biochemical properties of the leaf tissues in the initial stage of fungal infection [46], which could not be captured by traditional physiological and biochemical measurements, because the wet chemical analysis was based on the averaged responses of bulk leaf tissue. A previous study reported that PCR assay was very sensitive and accurate for confirming visual screening but was unreliable at the presymptomatic stage due to uneven pathogen distribution inside plants [11]. In contrast, the spectral reflectance signature corresponded to the subtle changes in the biochemical information and structural properties of the infected leaf tissue [10,16,20], and the high-resolution image dynamically reflected the heterogeneous spatial morphology at the pixel level when the mixed problem of the pixel spectrum was tackled with appropriate HSI unmixing analysis. This finding also highlights the importance of the spatial resolution of a proximal HSI sensing system in the detection and identification of leaf diseases, considering the mixed spectral signals from early

plant–pathogen interaction sites with small and subtle pathogenesis [21]. The effect of the spatial resolution of HSI on sensor sensitivity was confirmed in a small-scale analysis of disease symptoms of sugar beet [21].

In addition to the visualization of spatial heterogeneity of the plant–pathogen interaction sites, another advantage of HSI over traditional measurements lies in its capability to characterize the pathogenesis in the time dimension [10], due to its ability to perform repeated non-destructive monitoring over time, as displayed in Fig. 9. Similarly, the spatiotemporal heterogeneity of plant–pathogen interactions has been visualized in previous HSI studies on barley leaves, achieving presymptomatic detection at 4 dai [13], 4 dai [29], 2 dai [30], and 24 hai [31], respectively. However, the timelines of these diagnostic results were compared with those of visual inspection, without referring to PCR validation. It is notable that the presymptomatic diagnosis of spot blotch was ascertained using a PCR assay in this study. Spectral unmixing analysis has also been employed previously, but it was executed separately on hyperspectral images acquired at different infection times [31], and no FSSs that could capture the diseased lesions across different times were extracted. In this study, we improved the spectral unmixing results in extracting the FSSs, which gave three advantages: First, the extracted FSSs uniquely captured the characteristics of spot blotch lesions on *in vivo* leaves and were applicable to the time-series hyperspectral images across the early stages of disease infection. Second, in contrast to the selection of a few optimal discrete wavelengths for early disease diagnosis [23,25], the FSSs extracted herein spanned the continuous full-wavelength range. Since the biochemical and structural changes induced by the pathogens were complex and comprehensive, with multiple processes taking place, only full-spectrum FSSs could fully represent the spectral responses of the leaf tissues to disease. Also, compared with the few single bands provided in the previous literature, the full-spectrum FSSs were more robust to system noises. Third, the FSSs had definite physical interpretations corresponding to the biochemical and structural alterations of chlorotic and necrotic tissues, and the structural properties were also validated by microscopic observations of the infected leaf tissues (Fig. 8). Thus, the full-spectrum FSSs extracted in this study were representative, robust, and interpretable, and their time-series application permitted the *in situ* tracking of the spatiotemporal dynamics of plant–pathogen interactions for presymptomatic diagnosis. Moreover, in response to Mahlein et al.'s [10] call for acquired hyperspectral images to be linked to biological processes during plant–pathogen interactions, the diagnosis mechanism of HSI in association with the plant's biochemical responses, which had not yet been examined in the literature, required further investigation.

4.3. The mechanism of HSI presymptomatic diagnosis

Both the full-spectrum and the selected optimal characteristic wavelengths achieved good regression performance. Moreover, their correlations with the absorption of the chemical functional groups in the six biochemical components verified the spectroscopic quantification mechanism of these response indicators under spot blotch stress. Previous spectroscopic studies have also quantified the biochemical indicators of plants under stress. Yendrek et al. [54] established PLS prediction models of leaf chlorophyll, nitrogen, and sucrose contents using hyperspectral reflectance in order to assess the differences in biochemical responses to elevated O_3 across maize lines. The quantitative characterization of multiple biochemical indicators of tea seedlings, including pigments, moisture, and AsA under lead-containing aerosol particles stress, was carried out using spectroscopy [34].

The strong mathematical associations between the spectral responses and the host biochemical indicators indicated that the complex and comprehensive spatiotemporal dynamic changes in the biochemical and structural information of early-infected tissues [46] could be reflected in the continuous full-spectrum FSSs, explaining the effectiveness of the extracted FSSs for characterizing lesions over time. In addition, the biochemical information and structural characterization reflected by the spectral responses [20,49] are at the pixel level, considering the high spatial resolution of HSI. This revelation of the detection mechanism of FSSs makes HSI presymptomatic disease diagnosis better founded. Furthermore, the test of the VCA method on two other kinds of plant diseases demonstrated the remarkable generalization potential of the proposed combination of HSI technology and the VCA method for the early diagnosis of plant foliar diseases. In future work, these results will be evaluated at different scales (e.g., microscopic scale, canopy scale) to achieve improved scale-independent FSSs. Additional optical sensors (e.g., chlorophyll fluorescence) will be incorporated to enhance the capture of the characteristics of the lesions and link to additional biochemical indicators. This will provide state-of-the-art insights into and technologies for plant disease diagnosis and facilitate the accurate screening of plant resistance.

5. Conclusions

In this study, time-series hyperspectral images of *in vivo* barley leaves under spot blotch stress were acquired to characterize disease onset and development for rapid and *in situ* presymptomatic diagnosis at the pixel level. The early physiological and biochemical responses of barley leaves to disease stress were examined using traditional approaches, including PCR analysis of fungal colonization and determination of biochemical indicators (Chl-a, Chl-b, Car, AsA, GSH, and MDA). Both methods revealed significant differences between healthy and infected samples from 36 hai. For the *in situ* visualization of the plant–pathogen interactions, the spectral unmixing VCA method performed the best, extracting representative FSSs with abundance maps corresponding to the spatial distribution of healthy, slightly infected chlorotic, and severely infected necrotic mesophyll tissues. The structural properties of the three types of mesophyll tissues reflected by the FSSs in the near-infrared range were also validated using microscopic observations, which demonstrated the definite physical interpretation of the original HSI data by the extracted FSSs. The employment of FSSs on the repeatedly measured *in vivo* leaf samples made it possible to intuitively monitor the spatiotemporal dynamic heterogeneity at the early plant–pathogen interaction sites at the pixel level, demonstrating the applicability and robustness of the FSSs. This method enabled the presymptomatic diagnosis of spot blotch on barley leaves at 24 hai—12 h earlier than the traditional PCR or biochemical measurements. Finally, the mathematical relationships between the spectral responses and the biochemical indicators were established via regression models coupled with the identification and interpretation of optimal characteristic wavelengths. The quantification of these indicators achieved good modeling performances, with R_p^2 higher than 0.84 (Fig. S3), revealing the mechanism of presymptomatic diagnosis based on HSI and FSSs. The overall results demonstrated that, based on the association between HSI and *in vivo* plant-trait alterations, the extracted FSSs permitted the characterization of bipolaris spot blotch progression for presymptomatic diagnosis. Furthermore, the methodology was recognized to have remarkable generalization potential for the early control of plant diseases.

Acknowledgments

This research work was supported by the Key Research and Development Project of Zhejiang Province, China (2022C02044),

National Natural Science Foundation of China (32171889 and 32071895), the Natural Science Foundation of Zhejiang Province, China (LQ22C130004), and the National Key Research and Development Program of China (2018YFD0700501).

Authors' contribution

Fengle Zhu, Zhenzhu Su, Xiaoli Li, and Yong He conceived the study. Xiaoli Li acquired the funding. Zhenzhu Su, Ruiqing Zhou, Anand Babu Perumal, and Mostafa Gouda collected the experimental data. Alireza Sanaeifar, Ruiqing Zhou, Fengle Zhu, and Anand Babu Perumal contributed to the algorithm development and data analysis. Fengle Zhu, Zhenzhu Su, Alireza Sanaeifar, and Ruiqing Zhou contributed to the result interpretation. Fengle Zhu and Zhenzhu Su wrote the manuscript. Fengle Zhu, Alireza Sanaeifar, and Xiaoli Li contributed to the editing of the manuscript.

Compliance with ethics guidelines

Fengle Zhu, Zhenzhu Su, Alireza Sanaeifar, Anand Babu Perumal, Mostafa Gouda, Ruiqing Zhou, Xiaoli Li, and Yong He declare that they have no conflict of interest or financial conflicts to disclose.

Appendix A. Supplementary material

Supplementary data to this article can be found online at https://doi.org/10.1016/j.eng.2022.10.006.

References

[1] Kumar J, Schäfer P, Hückelhoven R, Langen G, Baltruschat H, Stein E, et al. *Bipolaris sorokiniana*, a cereal pathogen of global concern: cytological and molecular approaches towards better control double dagger. Mol Plant Pathol 2002;3(4):185–95.
[2] Novakazi F, Afanasenko O, Lashina N, Platz GJ, Snowdon R, Loskutov I, et al. Genome-wide association studies in a barley (*Hordeum vulgare*) diversity set reveal a limited number of loci for resistance to spot blotch (*Bipolaris sorokiniana*). Plant Breed 2020;139(3):521–35.
[3] Acharya K, Duta AK, Pradhan P. *Bipolaris sorokiniana* (Sacc.) Shoem.: the most destructive wheat fungal pathogen in the warmer areas. Aust J Crop Sci 2011;5 (9):1064–71.
[4] Gupta PK, Chand R, Vasistha NK, Pandey SP, Kumar U, Mishra VK, et al. Spot blotch disease of wheat: the current status of research on genetics and breeding. Plant Pathol 2018;67(3):508–31.
[5] Murray TD, Parry DW, Cattlin ND. A color handbook of diseases of small grain cereal crops. Ames: Iowa State University Press; 1998.
[6] Pandey SP, Kumar S, Kumar U, Chand R, Joshi AK. Sources of inoculum and reappearance of spot blotch of wheat in rice–wheat cropping systems in eastern India. Eur J Plant Pathol 2005;111(1):47–55.
[7] Sharma RC, Duveiller E. Advancement toward new spot blotch resistant wheats in South Asia. Crop Sci 2007;47(3):961–8.
[8] Kumar D, Chand R, Prasad LC, Joshi AK. A new technique for monoconidial culture of the most aggressive isolate in a given population of *Bipolaris sorokiniana*, cause of foliar spot blotch in wheat and barley. World J Microbiol Biotechnol 2007;23(11):1647–51.
[9] Al-Sadi AM. *Bipolaris sorokiniana*-induced black point, common root rot, and spot blotch diseases of wheat: a review. Front Cell Infect Microbiol 2021;11:584899.
[10] Mahlein AK, Kuska MT, Behmann J, Polder G, Walter A. Hyperspectral sensors and imaging technologies in phytopathology: state of the art. Annu Rev Phytopathol 2018;56(1):535–58.
[11] Martinelli F, Scalenghe R, Davino S, Panno S, Scuderi G, Ruisi P, et al. Advanced methods of plant disease detection. A review. Agron Sustain Dev 2015;35 (1):1–25.
[12] Lowe A, Harrison N, French AP. Hyperspectral image analysis techniques for the detection and classification of the early onset of plant disease and stress. Plant Methods 2017;13(1):80.
[13] Thomas S, Wahabzada M, Kuska MT, Rascher U, Mahlein AK. Observation of plant–pathogen interaction by simultaneous hyperspectral imaging reflection and transmission measurements. Funct Plant Biol 2016;44(1):23–34.
[14] Cen H, Weng H, Yao J, He M, Lv J, Hua S, et al. Chlorophyll fluorescence imaging uncovers photosynthetic fingerprint of citrus Huanglongbing. Front Plant Sci 2017;8:1509.
[15] Ghosal S, Blystone D, Singh AK, Ganapathysubramanian B, Singh A, Sarkar S. An explainable deep machine vision framework for plant stress phenotyping. Proc Natl Acad Sci USA 2018;115(18):4613–8.
[16] Abdulridha J, Ampatzidis Y, Qureshi J, Roberts P. Laboratory and UAV-based identification and classification of tomato yellow leaf curl, bacterial spot, and target spot diseases in tomato utilizing hyperspectral imaging and machine learning. Remote Sens 2020;12(17):2732.
[17] Das K, Roychoudhury A. Reactive oxygen species (ROS) and response of antioxidants as ROS-scavengers during environmental stress in plants. Front Environ Sci 2014;2:53.
[18] Kaur S, Bhardwaj RD, Kaur J, Kaur S. Induction of defense-related enzymes and pathogenesis-related proteins imparts resistance to barley genotypes against spot blotch disease. J Plant Growth Regul 2021;41(2):682–96.
[19] Zarco-Tejada PJ, Camino C, Beck PSA, Calderon R, Hornero A, Hernández-Clemente R, et al. Previsual symptoms of *Xylella fastidiosa* infection revealed in spectral plant-trait alterations. Nat Plants 2018;4(7):432–9.
[20] Zhang N, Yang G, Pan Y, Yang X, Chen L, Zhao C. A review of advanced technologies and development for hyperspectral-based plant disease detection in the past three decades. Remote Sens 2020;12(19):3188.
[21] Mahlein AK, Steiner U, Hillnhütter C, Dehne HW, Oerke EC. Hyperspectral imaging for small-scale analysis of symptoms caused by different sugar beet diseases. Plant Methods 2012;8(1):3.
[22] Bendel N, Backhaus A, Kicherer A, Köckerling J, Maixner M, Jarausch B, et al. Detection of two different grapevine yellows in *Vitis vinifera* using hyperspectral imaging. Remote Sens 2020;12(24):4151.
[23] Shuaibu M, Lee WS, Schueller J, Gader P, Hong YK, Kim S. Unsupervised hyperspectral band selection for apple Marssonina blotch detection. Comput Electron Agric 2018;148:45–53.
[24] Arens N, Backhaus A, Döll S, Fischer S, Seiffert U, Mock HP. Non-invasive presymptomatic detection of *Cercospora beticola* infection and identification of early metabolic responses in sugar beet. Front Plant Sci 2016;7:1377.
[25] Gao Z, Khot LR, Naidu RA, Zhang Q. Early detection of grapevine leafroll disease in a red-berried wine grape cultivar using hyperspectral imaging. Comput Electron Agric 2020;179:105807.
[26] Abdulridha J, Ampatzidis Y, Roberts P, Kakarla SC. Detecting powdery mildew disease in squash at different stages using UAV-based hyperspectral imaging and artificial intelligence. Biosyst Eng 2020;197:135–48.
[27] Abdulridha J, Ampatzidis Y, Kakarla SC, Roberts P. Detection of target spot and bacterial spot diseases in tomato using UAV-based and benchtop-based hyperspectral imaging techniques. Precis Agric 2020;21(5):955–78.
[28] Thomas S, Behmann J, Steier A, Kraska T, Muller O, Rascher U, et al. Quantitative assessment of disease severity and rating of barley cultivars based on hyperspectral imaging in a non-invasive, automated phenotyping platform. Plant Methods 2018;14(1):45.
[29] Kuska M, Wahabzada M, Leucker M, Dehne HW, Kersting K, Oerke EC, et al. Hyperspectral phenotyping on the microscopic scale: towards automated characterization of plant–pathogen interactions. Plant Methods 2015;11 (1):28.
[30] Kuska MT, Brugger A, Thomas S, Wahabzada M, Kersting K, Oerke EC, et al. Spectral patterns reveal early resistance reactions of barley against *Blumeria graminis* f. sp. *hordei*. Phytopathology 2017;107(11):1388–98.
[31] Zhou RQ, Jin JJ, Li QM, Su ZZ, Yu XJ, Tang Y, et al. Early detection of *Magnaporthe oryzae*-infected barley leaves and lesion visualization based on hyperspectral imaging. Front Plant Sci 2019;9:1962.
[32] Zhu F, Zhang D, He Y, Liu F, Sun DW. Application of visible and near infrared hyperspectral imaging to differentiate between fresh and frozen–thawed fish fillets. Food Bioprocess Technol 2013;6(10):2931–7.
[33] Wellburn AR, Lichtenthaler H. Formulae and program to determine total carotenoids and chlorophylls A and B of leaf extracts in different solvents. In: Proceedings of the VIth International Congress on Photosynthesis; 1983 Aug 1–6; Brussels, Belgium. Netherlands: Springer; 1984. p. 9–12.
[34] Sanaeifar A, Zhu F, Sha J, Li X, He Y, Zhan Z. Rapid quantitative characterization of tea seedlings under lead-containing aerosol particles stress using Vis-NIR spectra. Sci Total Environ 2022;802:149824.
[35] Chen HZ, Zhang M, Guo Z. Discrimination of fresh-cut broccoli freshness by volatiles using electronic nose and gas chromatography-mass spectrometry. Postharvest Biol Technol 2019;148:168–75.
[36] Livak KJ, Schmittgen TD. Analysis of relative gene expression data using real-time quantitative PCR and the $2^{-\Delta\Delta Ct}$ method. Methods 2001;25(4):402–8.
[37] Deshmukh S, Hückelhoven R, Schäfer P, Imani J, Sharma M, Weiss M, et al. The root endophytic fungus *Piriformospora indica* requires host cell death for proliferation during mutualistic symbiosis with barley. Proc Natl Acad Sci USA 2006;103(49):18450–7.
[38] Deshmukh SD, Kogel KH. *Piriformospora indica* protects barley from root rot caused by *Fusarium graminearum*. J Plant Dis Prot 2007;114(6):263–8.
[39] Macqueen J. Some methods for classification and analysis of multivariate observations. Proceedings of the Fifth Berkeley Symposium on Mathematical Statistics and Probability, 1967; Oakland, CA, USA. Cambridge: Cell Press; 1969.
[40] Bezdek JC, Ehrlich R, Full W. FCM: the fuzzy *c*-means clustering algorithm. Comput Geosci 1984;10(2–3):191–203.
[41] Keshava N, Mustard JF. Spectral unmixing. IEEE Signal Process Mag 2002;19 (1):44–57.
[42] Nascimento JMP, Dias JMB. Vertex component analysis: a fast algorithm to unmix hyperspectral data. IEEE Trans Geosci Remote Sens 2005;43 (4):898–910.
[43] Huang Y, Dong W, Sanaeifar A, Wang X, Luo W, Zhan B, et al. Development of simple identification models for four main catechins and caffeine in fresh

green tea leaf based on visible and near-infrared spectroscopy. Comput Electron Agric 2020;173:105388.
[44] Liu Z, Cai W, Shao X. Outlier detection in near-infrared spectroscopic analysis by using Monte Carlo cross-validation. Sci China B Chem 2008;51(8):751–9.
[45] Maldonado AIL, Rodriguez-Fuentes H, Contreras JAV. Hyperspectral imaging in agriculture, food and environment. London: IntechOpen; 2018.
[46] Tian L, Xue B, Wang Z, Li D, Yao X, Cao Q, et al. Spectroscopic detection of rice leaf blast infection from asymptomatic to mild stages with integrated machine learning and feature selection. Remote Sens Environ 2021;257:112350.
[47] Leucker M, Wahabzada M, Kersting K, Peter M, Beyer W, Steiner U, et al. Hyperspectral imaging reveals the effect of sugar beet quantitative trait loci on *Cercospora* leaf spot resistance. Funct Plant Biol 2017;44(1):1.
[48] Krinidis S, Chatzis V. A robust fuzzy local information *c*-means clustering algorithm. IEEE Trans Image Process 2010;19(5):1328–37.
[49] Ollinger SV. Sources of variability in canopy reflectance and the convergent properties of plants. New Phytol 2011;189(2):375–94.
[50] Cen H, He Y. Theory and application of near infrared reflectance spectroscopy in determination of food quality. Trends Food Sci Technol 2007;18(2):72–83.
[51] Walsh KB, Blasco J, Zude-Sasse M, Sun X. Visible-NIR 'point' spectroscopy in postharvest fruit and vegetable assessment: the science behind three decades of commercial use. Postharvest Biol Technol 2020;168:111246.
[52] Able AJ. Role of reactive oxygen species in the response of barley to necrotrophic pathogens. Protoplasma 2003;221(1–2):137–43.
[53] Yusuf CS, Chand R, Mishra VK, Joshi AK. The association between leaf malondialdehyde and lignin content and resistance to spot blotch in wheat. J Phytopathol 2016;164(11–12):896–903.
[54] Yendrek CR, Tomaz T, Montes CM, Cao Y, Morse AM, Brown PJ, et al. High-throughput phenotyping of maize leaf physiological and biochemical traits using hyperspectral reflectance. Plant Physiol 2017;173(1):614–26.